

ARTICLE

Syngas Molecules as Probes for Defects In 2D Hexagonal Boron Nitride: their Adsorption and Vibrations

Tao Jiang,^a Duy Le,^{a,b} Takat B. Rawal,^{a,†} and Talat S. Rahman^{a,b,*}

Received 00th January 20xx,
Accepted 00th January 20xx

DOI: 10.1039/x0xx00000x

Single-layer, defect-laden hexagonal boron nitride (*dh*-BN) is attracting a great deal of attention for its diverse applications: catalysis on the one hand, and single photon emission on the other. As possible probes for identifying some common defects in single-layer *h*-BN, we present results of *ab initio* calculations for the adsorption and vibrational characteristics of syngas molecules (H₂, CO, CO₂) on *dh*-BN containing one of four types of defects: nitrogen vacancy (V_N), boron vacancy (V_B), Stone–Wales defect (SW), and nitrogen substituted by boron (B_N). Through a comparative examination of adsorption features, charge transfer, electronic structure, and vibrational spectrum, we obtain a deep understanding of the interaction of these molecules with *dh*-BN and the role of the defect states. We find that while CO and CO₂ chemisorb, molecular H₂ physisorbs, but dissociative adsorption of H₂ is feasible on *dh*-BN. V_N and V_B show strong affinity for CO and CO₂ since the defect states induced by them lie close to the Fermi level. SW does not favor adsorption of these small molecules, as the process for each is endothermic. At B_N CO adsorbs strongly but CO₂ only weakly. Vibrational frequencies of notable modes localized at the adsorbed molecules are analyzed and suggested as measures for identification of the defect type. Systematically investigating the adsorption of small molecules on these defects, we predict that *dh*-BN with V_N is a good catalyst candidate for CO₂ hydrogenation.

Introduction

Similar to other two dimensional (2D) materials, single-layer hexagonal boron nitride (*h*-BN) has received considerable attention in the past few years owing to its novel properties that make it amenable for various applications.¹ Structurally analogous to graphene, single-layer *h*-BN has B and N atoms arranged in a hexagonal lattice and bound together by strong covalent bonds. It is a wide bandgap material with the high chemical stability² and ideally suited as a reliable support for other 2D materials.³ Its unique properties have also suggested its potential usage in optoelectronics⁴ and photo-catalysis.⁵ Even more remarkable have been the recent findings of its suitability as a catalyst^{1, 6, 7} and as single photon emitter,^{8–10} raising questions about the role of defects. This is to be expected as pristine *h*-BN is chemically inert because of the lack of dangling bonds.¹¹ It therefore calls for prudent ways to activate the basal plane of *h*-BN. Taking cues from prior studies on MoS₂,^{12–17} proposals have been made to activate the basal plane on *h*-BN by the creation of defects,^{18, 19} deposition of metal atoms or molecules,^{20–23} creation of grain-boundaries,²⁴ and application of strain to the defective surface.²⁵ Quite akin to defect-laden single-layer MoS₂ (with sulfur vacancies), which

calculations predict to be a possible catalyst for hydrogenation of syngas to alcohol,¹² the basal plane of the single-layer *h*-BN can be chemically activated for similar reaction, in the presence of point or line defects on the surface. Indeed, in the above mentioned experimental and theoretical study⁶ showing propane hydrogenation, the activity was traced to the presence of defects. While nitrogen vacancy has been proposed as the most active defect, interestingly for both catalytic⁶ and single-photon emissive⁸ properties, the role of other types of defects cannot be ruled out. Defects are, however, not easy to characterize experimentally, notwithstanding the nanometer resolution scanning tunneling microscopy (STM) studies by Feng et al.⁹ Small molecules such as H₂, CO, CO₂, the syngas trio, could serve as probe of defects through their adsorption and vibrational characteristics on *dh*-BN.

Beyond serving as probes of defects, an in-depth understanding of the relative propensity of common defect types in facilitating adsorption of syngas molecules on *dh*-BN is the first step in rational designing of *dh*-BN for specific hydrogenation reactions. The topic is of broad interest since *h*-BN is readily available and thermally stable. With appropriate defects it could serve as a metal-free catalyst for hydrogenation of CO/CO₂ even at ambient or higher temperatures. To probe the catalytic properties of *h*-BN toward such hydrogenation, it is thus essential that we gain fundamental insights into the interactions between *h*-BN and syngas, as presented in this work. It should be noted that adsorption of H₂, CO, and CO₂ (syngas) on solid catalyst materials are the fundamental processes and the starting points of the reaction pathway of their conversion into useful (value-added) chemical products, i.e., simple to higher

^a Department of Physics, University of Central Florida, Orlando, FL, 32816 USA

^b Renewable Energy and Chemical Transformations Cluster, University of Central Florida, Orlando, FL, 32816 USA

*Email: talat.rahman@ucf.edu

[†]Present address: Department of Physics, University of Houston, Houston, TX 77204 USA

alcohols, formaldehyde, formic acid, and higher hydrocarbons.²⁶⁻²⁸ The thermodynamic favorability and kinetic stability of the adsorption of syngas molecules on the catalyst surface are critical for efficiently and selectively promoting hydrogenations of CO and CO₂.²⁹ In fact, it requires an appropriate catalyst material which should be thermally stable, chemically active and selective for the desired reaction products. Historically, metal-based catalysts have been widely investigated and utilized for hydrogenation reaction, as they typically demonstrate good catalytic activity and product selectivity.²⁶⁻²⁸ The optimal catalyst material is, however, often an expensive, non-abundant metal and/or can be easily oxidized and deactivated. Copper-based catalysts²⁸ are not expensive but they have poor thermal stability, and hence not suitable for high-temperature reactions without a thermal stabilizer. Cerium-based catalysts³⁰ have also shown good activity and selectivity for CO₂ hydrogenation process, but are easily deactivated by a small coverage of deposited carbon. There is thus a need to develop cost-effective catalyst material which has superior properties for syngas conversion than presently available.

With the above in mind, we present here results of *ab initio* calculations, based on density functional theory (DFT) of the adsorption of syngas on the *dh*-BN layer with one of four possible types of defects - nitrogen vacancy (V_N), boron vacancy (V_B), stone-wales (SW), and nitrogen substituted by boron (B_N) - which have been shown to have affinity towards the selected adsorbates.⁶ To probe the reactivity of single-layer *h*-BN with these defects, we compare the adsorption and vibrational characteristics of syngas molecules on them. We examine the favorable sites and orientation of these molecules on *dh*-BN and analyze the unique local atomic environment and electronic structure of *dh*-BN as modified by the adsorbed molecules (H₂, CO and CO₂). Quite importantly, we calculate and analyze vibrational frequencies of modes localized at the adsorbed molecules and nearby defect sites to identify notable vibrational frequencies as possible signatures of the adsorption, and thereby the defect type. Based on the DFT-calculated energetics for syngas-adsorption, we show that the *h*-BN with nitrogen vacancy may serve as a potential metal-free catalyst material for hydrogenation of CO₂.

In the next section, we introduce details of our computational methodology. We next presents results and discussion, starting with the geometrical and electronic structure of the four types of point defects in *h*-BN considered in this work, followed by the adsorption and vibrational analysis of H₂, CO, and CO₂ on the defects and the discussion of implication of our results towards the catalytic activity of *h*-BN. Finally, we provide main conclusions of this work.

Computational details

All calculations are performed by using spin-polarized DFT, implemented in the Quantum Espresso Code,³¹ employing plane-wave basis set and the projected-augmented-wave (PAW) method^{32, 33} for interaction between electrons and nuclei. We use the vdW-DF2 functional³⁴ for exchange-

correlation of electrons as it is found to produce excellent lattice constant of *h*-BN. We use the plane wave basis set with kinetic energy cutoff of 45 Ry and charge density with 180 Ry. We construct a (6×6) supercell of single layer hexagonal boron nitride (*h*-BN) with periodic boundary conditions along in-plane directions and a vacuum of 20 Å to avoid the spurious interaction between periodical images. To model a defect-laden *h*-BN system (so-called *dh*-BN), we remove either a boron/nitrogen atom or substitute a nitrogen atom by a boron atom or rotate a B-N bond by 90 degree. The relaxed structures of our model systems of *h*-BN with various defects, namely, nitrogen vacancy (V_N), boron vacancy (V_B), Stone Wales defect (SW) and nitrogen substituted by boron (B_N) are shown in Figure 1. To investigate the adsorption characteristics of H₂, CO and CO₂ we place single molecule at the defect site and at the neighboring atoms near defect sites (We will present only the lowest-energy adsorption structures). All systems are relaxed until their energy converges to 10⁻⁶ eV and the residual force on each atom reaches below 0.005 eV/Å. For calculations of geometry relaxation, we sample the Brillouin zone with one point at the zone center and for electronic density of states, we use a 12×12×1 k-point mesh.

The adsorption energy is defined as $E_{\text{ads}} = E_{\text{Molecule/dh-BN}} - (E_{\text{Molecule}} + E_{\text{dh-BN}})$, where, $E_{\text{Molecule/dh-BN}}$, E_{Molecule} , $E_{\text{dh-BN}}$ are the total energy of the molecule on *dh*-BN, isolated molecule, and *dh*-BN system, respectively. We calculate charge density difference upon adsorption of molecules on *dh*-BN using: $\Delta\rho = \rho_{\text{Molecule/dh-BN}} - (\rho_{\text{Molecule}} + \rho_{\text{dh-BN}})$, where $\rho_{\text{molecule/dh-BN}}$, $\rho_{\text{dh-BN}}$, and ρ_{Molecule} are charge density of the molecule on *dh*-BN, *dh*-BN itself, and the isolated molecule, respectively. We calculate charge on each atom using Bader charge analysis^{35, 36} which allows estimation of the charge transfer between the molecule and *dh*-BN. Vibration frequencies were calculated using the finite-difference method as implemented in the Phonopy package,³⁷ in which we use a displacement of 0.01 Å to maintain the validity of the harmonic approximation and avoid numerical errors that would otherwise introduce chaotic behavior in the result. Zero point energy (ZPE) correction for the total energy of each system is calculated as $\sum_{i=1}^N \hbar\nu_i/2$, where \hbar is the Planck constant, ν_i is the frequency of vibrational mode i ($i = 1..N$, where N is the total number of vibrational modes of the system).

Results and Discussions

Geometrical and Electronic Structure of dh-BN

We present in Figure 1 the geometry of the considered four types of defect in single-layer *h*-BN, V_N, V_B, SW, and B_N. To explore their electronic structure, we show the spin dependent density of states of each defect in Figure 2.

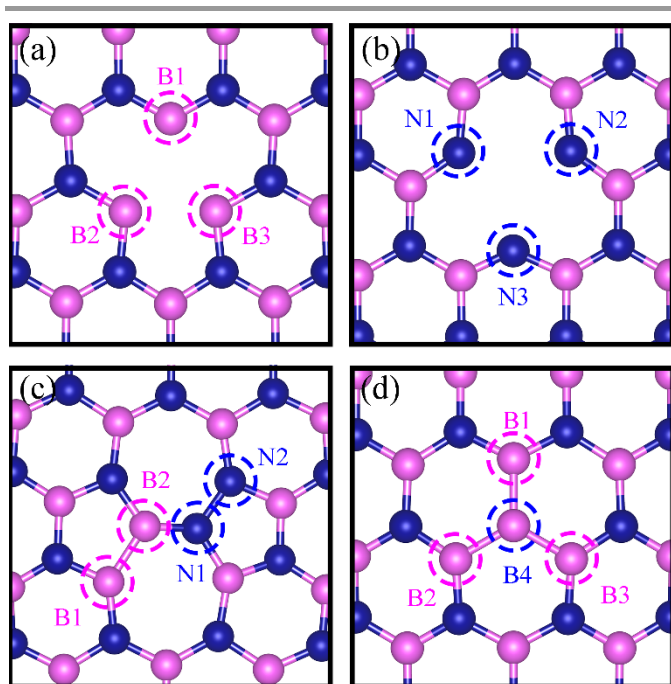


Figure 1 Schematic representation of *h*-BN model systems with defects: (a) V_N , (b) V_B , (c) SW, and (d) B_N . Blue and magenta balls represent N and B atoms, respectively.

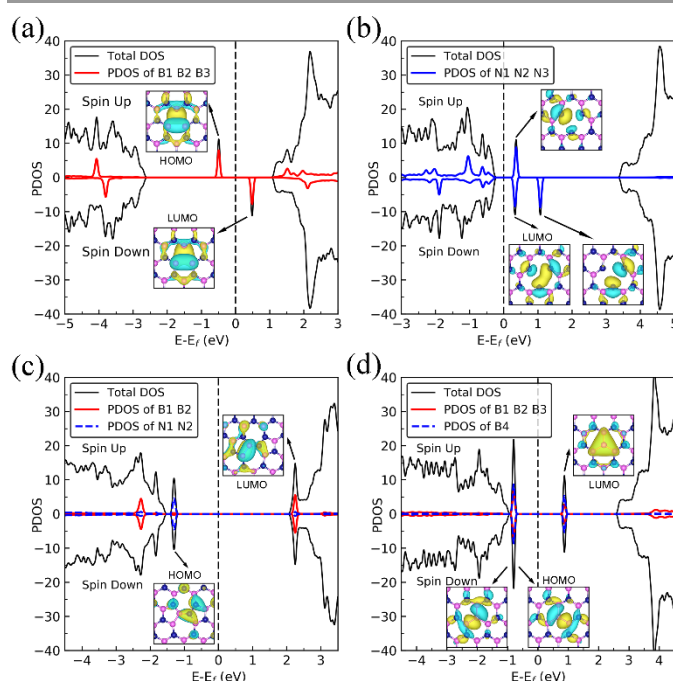


Figure 2 Spin-polarized projected density of states (PDOS) of *dh*-BN with defects: (a) V_N , (b) V_B , (c) SW, and (d) B_N . The inset displays the wave function of the defect states with isosurface value of $0.001 |e|/\text{Å}$.

Nitrogen vacancy (V_N)

The presence of a nitrogen vacancy on the *h*-BN surface leads to a local geometrical change (Figure 1a) as reflected by changes in the bond lengths and bond angles. The distance between B and N atoms ($d_{(B_2-N)}$) is 1.492 Å , to be compared to 1.454 Å of

the pristine *h*-BN, whereas the angle between N, B and N atoms ($\theta_{(N-B_2-N)}$) is 113.6° as opposed to 120° in pristine *h*-BN. Also, the separation between N atoms, $d_{(N-N)}$, is changed from 2.485 to 2.471 Å (0.5% change).

From spin-polarized calculations of electronic density of states in Figure 2a, we find that *dh*-BN (V_N) is a spin-polarized system - the effect arising from the unpaired electrons produced by the N vacancy. Of critical importance are the two mid-gap states, one is spin-up - the highest occupied molecular orbital (HOMO) - and the other is spin-down - the lowest unoccupied molecular orbital (LUMO). These states are separated by 0.98 eV . The wave functions of HOMO and LUMO (Inserts in Figure 2a) adapt the same symmetry and are π -type orbitals, which are localized at the vacancy, i.e., at the B1, B2, B3 atoms (shown in Figure 1a) and surrounding the N and B atoms. The mid-gap states are mostly contributed from B1, B2, and B3 atoms, as shown in Figure 2a.

Boron vacancy (V_B)

The existence of a boron vacancy on single-layer *h*-BN leads to the following geometrical change at the defect (Figure 1b): as compared to those in pristine *h*-BN, the distance between N and B atoms ($d_{(B-N_1)}$) shortens from 1.455 Å to 1.419 Å (2.5% change); the angle between B, N and B atoms ($\theta_{(B-N_1-B)}$) enlarges from 120° to 129.3° (7.8% change); and the distance between N atoms, i.e. $d_{(N-N)}$, elongates from 2.520 Å to 2.565 Å (1.8% change). The *dh*-BN with V_B also possesses spin-polarized electronic DOS, as indicated by the calculated spin-up and -down DOS shown in Figure 2b. The presence of B vacancy leads to unsaturation of the bonds for the nearest-neighboring N (N1, N2, and N3) atoms. As shown in the inset in Figure 2b, the LUMO orbital in the spin-down channel is a σ -type orbital, located near the valence band edge of *h*-BN. As indicated in PDOS of N1/N2/N3 atoms (blue curve Figure 2b), the LUMO and two other mid-gap states (above LUMO, one is spin up and the other is spin down) are mainly composed of the states of N1/N2/N3 atoms, which is similar to the results of Huang et al.¹⁸

Stone-Wales (SW) Defect

The Stone-Wales (SW) defect is created by rotation of a B-N bond by 90° around its midpoint, as shown in Figure 1c. The bond lengths of B1-B2, B2-N1, N1-N2 are found to be 1.686 Å , 1.375 Å and 1.478 Å , respectively. The PDOS of *dh*-BN (SW), shown in Figure 2c, indicates that occupied and unoccupied defect states are not spin-polarized. The unoccupied defect states (LUMO) above the Fermi level are mainly contributed by the B1 and B2 atoms with a small contribution from the atoms surround B1 and B2 atoms while the occupied defect states (HOMO) below the Fermi level have main contributions from N1 and N2 atoms. The LUMO states are σ -type dominated by p_x and p_y orbitals from the B-B bond, while the HOMO states are π -type, in agreement with Ref. [38].

B substitution for N (B_N)

B_N defects are formed by the substitution of a B atom for a N atom at the lattice of pristine *h*-BN as shown in Figure 1d. The bond lengths of B-B and N-B are found to be 1.627 Å , 1.452 Å , respectively. The PDOS plot, Figure 2d, obtained for *dh*-BN with B_N clearly displays its large bandgap with non-spin-polarized

defect-related gap states. Since boron has two fewer valence electrons than nitrogen, dangling bonds are formed. In the defect levels below and above the Fermi level, atom B4 makes larger contribution than the sum of the contributions from atoms B1, B2, and B3. Note that H. Choi et al.³⁹ have already analyzed electronic properties of boron nitride nanotube with B_N. In our case, the B4 atoms and its surrounding boron atoms of the single layer *dh*-BN (B_N) resemble the geometry in the boron nitride nanotube with B_N, indicating similar electronic properties of B_N. We also find that the B_N defect introduces unoccupied defect states (LUMO) in the middle of the energy gap and occupied defect states (HOMO) near the valence band edge. These are σ -type orbitals with similar geometric structure in comparison with those in the nanotube with B_N.³⁹

Adsorption of small molecules on *dh*-BN

Hydrogen molecule on *dh*-BN

Figure 3 shows the optimized geometries of H₂ on *dh*-BN with V_N, V_B, SW and B_N. We find that H₂ molecule only physisorbs on single layer *dh*-BN with the adsorption energy of -0.07 eV, +0.08 eV, -0.08 eV and -0.08 eV, at V_N, V_B, SW and B_N, respectively. The bond length of H-H of H₂ on all four defects is 0.737 Å, which is almost identical to H-H bond length of 0.735 Å in the gas phase. The distance d_(H-B) for H₂ is 3.359 Å, 3.267 Å, and 3.357 Å, on V_N, SW and B_N, respectively. The distance d_(H-N) for H₂ on V_B is 3.285 Å. Electron transfer from the *dh*-BN to H₂ molecules is found to be negligible (0.005, 0.004, 0.002, and 0.004 e, on V_N, V_B, SW and B_N, respectively). Such small electron transfer reflects the fact that the H₂ molecule is physisorbed on *dh*-BN, consistent with almost-unchanged H-H bond lengths.

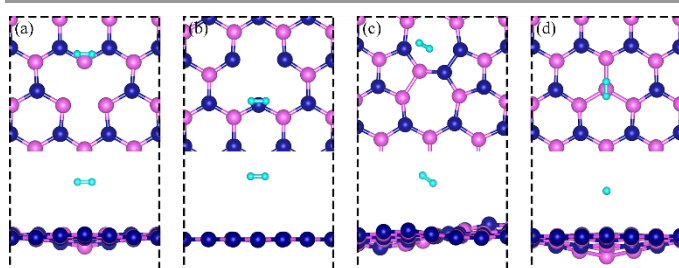


Figure 3 Optimized structures of H₂ adsorbed at favored sites of *dh*-BN with a) V_N, b) V_B, c) SW, and d) B_N. The magenta, blue, white balls represent the B, N and H atoms, respectively. The top and bottom panel shows the top and side views, respectively.

Adsorption of two Atomic Hydrogens on *dh*-BN

Since H₂ does not chemisorb in molecular form on *dh*-BN with V_N, V_B, SW and B_N, we turn to investigate the adsorption of the molecule in the form of two atomic hydrogens on *dh*-BN. Binding geometries of two adsorbed atomic hydrogens (2H) on the four considered types of *dh*-BN substrates are shown in Figure 4. The geometries of the most stable adsorption sites are similar to those in previous work by Nash. et al.⁶ The calculated energetic and geometric parameters, including the adsorption energy, H-H distance, and the distance of formed B(N)-H bond, are summarized in Table 1.

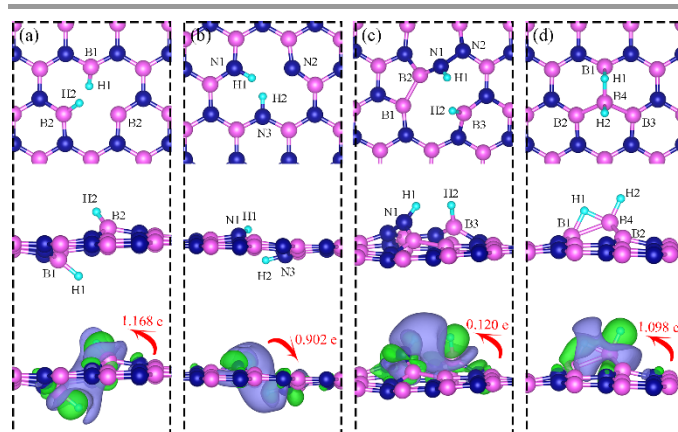


Figure 4 Optimized structures of two hydrogen atoms adsorbed at energetically favorable sites on single layer *dh*-BN with a) V_N, b) V_B, c) SW, and d) B_N. The magenta, blue, cyan balls represent the B, N and H atoms, respectively. The top and middle panel shows the top and side views, respectively. Bottom panel: the corresponding side views of the geometric structures with the charge density difference plot. The green and violet isosurfaces with isovalue of ± 0.003 e/Å³, represent the accumulation and depletion of charge, respectively. The red arrow shows the direction of electron transfer evaluated with Bader charge analysis.

Table 1 The adsorption energy without (E_{ads}) and with (E'_{ads}) ZPE correction, geometrical parameters, and notable frequencies for adsorption of 2 atomic Hydrogen on *dh*-BN.

Defects	Sites	E_{ads} (eV)	E'_{ads} (eV)	Distance between atoms (Å)	Notable frequencies (cm ⁻¹)
V _N	B1, B2	-1.61	-1.32	$d_{(\text{H-H})}=3.087$, $d_{(\text{H1-B1})}=1.189$, $d_{(\text{H2-B2})}=1.190$	2550.4 cm ⁻¹ , 2554.5 cm ⁻¹
V _B	N1, N2	-4.61	-4.13	$d_{(\text{H-H})}=1.869$, $d_{(\text{H1-N1})}=1.012$, $d_{(\text{H2-N2})}=1.009$	3446.24 cm ⁻¹ , 3502.9 cm ⁻¹
SW	B3, N1	+1.16	1.41	$d_{(\text{H-H})}=1.687$, $d_{(\text{H1-N1})}=1.004$, $d_{(\text{H2-B3})}=1.190$, $d_{(\text{B3-N1})}=2.632$	2543.6 cm ⁻¹ , 3572.7 cm ⁻¹
B _N	B1, B4	-1.51	-1.35	$d_{(\text{H-H})}=1.757$, $d_{(\text{H1-B4})}=1.207$, $d_{(\text{H2-B4})}=1.274$, $d_{(\text{H2-B2})}=1.315$, $d_{(\text{B1-B4})}=1.858$	2051.7 cm ⁻¹ , 2440.0 cm ⁻¹

On *dh*-BN with V_N, two hydrogen atoms (2H) prefer to bind to B atoms near N vacancy such that they (2H) are on the opposite side of the *dh*-BN sheet and the difference in their z coordinates is 2.934 Å (Figure 4a). The adsorption energy of 2H is found to be -1.61 eV. On *dh*-BN with V_B, shown in Figure 4b, 2H prefer to attach to N atoms near the B vacancy in such a way that the two H atoms are on the opposite side of the sheet with a difference in their z-position of 1.490 Å. The adsorption energy of 2H on *dh*-BN with V_B is -4.61 eV, an extremely exothermic adsorption. For the case of two hydrogens adsorption on *dh*-BN with SW, the H atoms prefer to stay on the same side of SW as shown in Figure 4c, in which one hydrogen attaches to B3 while the other attaches to N1. We find that the adsorption of 2 H atoms on SW breaks the bond of B3-N1, with the distance $d_{(\text{B3-N1})}$ of 2.632 Å, largely increased from 1.487 Å in the absence of the H atoms. This adsorption is endothermic with energy of +1.16 eV, the

positive sign signifying that it is not favored, mainly because there is no undercoordinated site at the SW. For the case of 2H adsorption on *dh*-BN with B_N , one hydrogen prefers to adsorb on the center boron atom (B4) whereas the other prefers to stay at the bridge between B1 and B4, as shown in Figure 4d. The adsorption energy of this configuration is -1.51 eV.

Charge density difference (CDD) plots, shown in the bottom panels of Figure 4, indicate noticeable rearrangement of electron density and electron transfer. For V_N and B_N , the *dh*-BN donates 1.168 e and 1.098 e to the atomic hydrogens, respectively. For V_B , the defect gains 0.902 e from atomic hydrogens. In the case of SW, there is 0.120 e transferring from *dh*-BN to atomic hydrogens. We also find that the adsorption of 2 H has effect on the electronic density of states of *dh*-BN (Figure 5). Overall, our calculations indicate that atomic hydrogen atoms adsorb most strongly on *dh*-BN with a V_B defect ($E_{\text{ads}} = -4.73$ eV) and not at all when the defect is SW ($E_{\text{ads}} = +1.04$ eV). The inclusion of zero-point energy correction changes the binding energy of 2H to *dh*-BN to -1.32, -4.13, +1.41, and -1.35 eV with V_N , V_B , SW, and B_N , respectively,

The adsorption of H on the defects create either B-H, N-H, or both on the *dh*-BN sheets. The vibrational frequencies of the stretching mode of the bonds should play an important role in determining the defect sites to which H adsorbs to. The notable vibrational frequencies of such modes are listed in Table 1 and their corresponding vibrational pattern are shown in Figure 6.

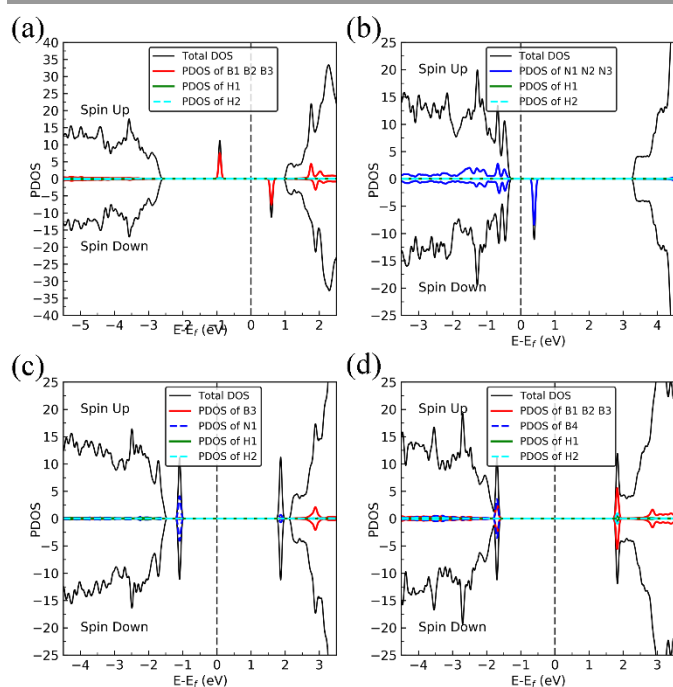


Figure 5 Spin-polarized total density of states (TDOS) (black line), spin-polarized PDOS of defect area in (red line or blue line) and spin-polarized PDOS adsorbed two hydrogens (green line and cyan line) of 2H-*dh*-BN with (a) V_N , (b) V_B , (c) SW, and (d) B_N , respectively. The position of the Fermi level (E_F) is indicated by dashed line.

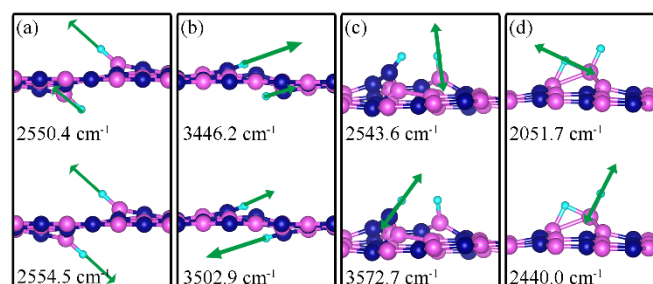


Figure 6 Notable vibration pattern of two hydrogen atoms adsorbed on *dh*-BN with a) V_N , b) V_B , c) SW, and d) B_N defect. The magenta, blue, black and light blue balls represent the B, N, and H atoms, respectively. Arrows indicate displacement directions.

CO on *dh*-BN

Carbon monoxide (CO) is one of the major common toxic gases in the atmosphere and is the main component of syngas, the essential reactant for (higher) alcohol synthesis. Figure 7 shows the geometric structure of the lowest energy configuration of CO adsorption on the V_N , V_B , SW, and B_N . Table 2 summarizes the binding energy, geometric parameters, and notable frequencies for the CO binding on the four types of defects in *h*-BN.

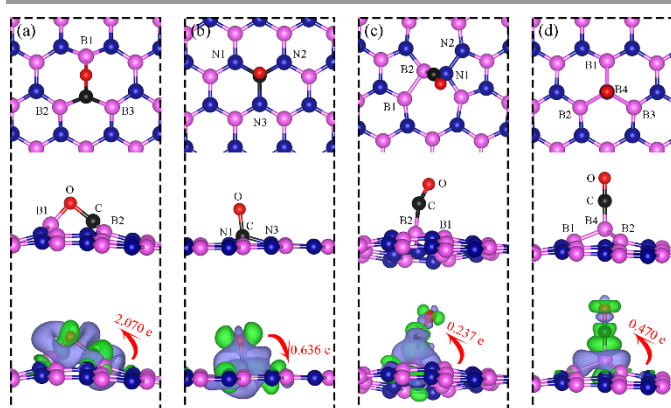


Figure 7 Top and side views of the most energetically favorable configurations of adsorbed CO on *dh*-BN with a) V_N , b) V_B , c) SW, and d) B_N type defect. The magenta, blue, black and red balls represent the B, N, C, and O atoms, respectively. The top and middle panel shows the top and side views, respectively. Bottom: the corresponding side views of the geometric structures with the charge density difference. The green and violet isosurfaces with iso-value of ± 0.003 e/ \AA^3 , represent the accumulation and depletion of electron, respectively. The red arrow shows the electron transfer in direction and value using Bader charge analysis.

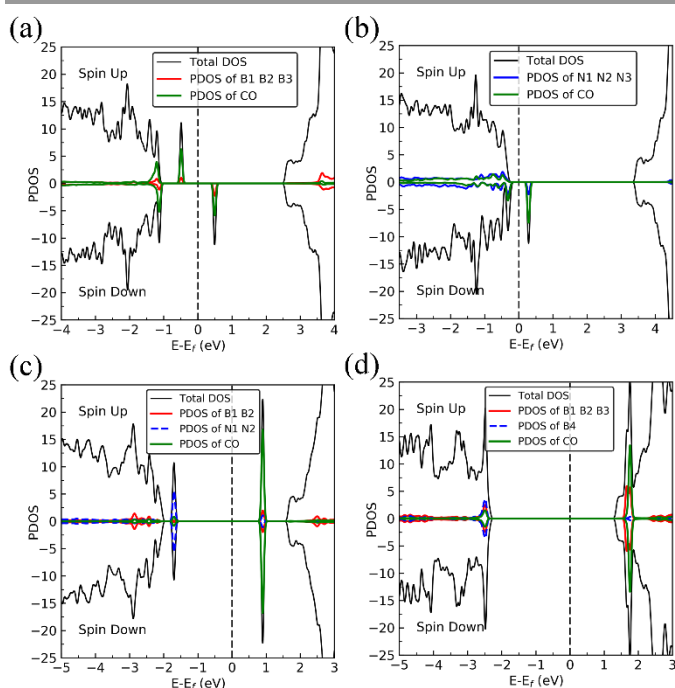


Figure 8 Spin-polarized total density of states (TDOS) (black line), spin-polarized PDOS of defect area in (red line or blue line) and spin-polarized PDOS adsorbed CO (green line) of CO-*dh*-BN with (a) V_N , (b) V_B , (c) SW, and (d) B_N , respectively. The position of the Fermi level (E_F) is indicated by dashed line.

Table 2 The adsorption energy without (E_{ads}) and with (E'_{ads}) ZPE correction, geometrical parameters, and notable frequencies for adsorption of CO on *dh*-BN.

Defects	E_{ads} (eV)	E'_{ads} (eV) ZPE	Bond length (Å) and Bond angle (°)	Notable frequencies (cm^{-1})
V_N	-3.45	-3.24	$d_{(\text{C-O})}=1.403$, $d_{(\text{C-B1})}=1.528$, $d_{(\text{O-B1})}=1.417$, $\theta_{(\text{C-O-B1})}=93.5^\circ$	333.9, 349.6, 1063.6
V_B	-4.54	-4.31	$d_{(\text{C-O})}=1.386$, $d_{(\text{C-N1})}=1.493$, $\theta_{(\text{O-C-N1})}=103.9^\circ$	117.3, 141.6, 895.5, 971.8, 973.5
SW	0.43	0.44	$d_{(\text{C-O})}=1.150$, $d_{(\text{C-B2})}=1.636$, $\theta_{(\text{O-C-B2})}=159.0^\circ$	54.2, 243.1, 397.9, 1986.9
B_N	-2.53	-2.45	$d_{(\text{C-O})}=1.163$, $d_{(\text{C-B4})}=1.444$, $\theta_{(\text{B4-C-O})}=179.9^\circ$	43.4, 46.7, 266.6, 467.1, 469.0, 1999.5

CO adsorption on V_N

On V_N , CO binds at the defect sites with O atom bonded to B1 atom and C atom bonded to two B2 and B3, as shown in Figure 7a, agree with previously reported results.^{40, 41} The adsorption causes out-of-plane displacement of the B1 atom by about 1 Å, which is quite large. The CO bond length increases from 1.134 Å (gas phase) to 1.403 Å (adsorbed), while $d_{(\text{C-B2})}$ ($d_{(\text{C-B3})}$) and $d_{(\text{O-B})}$ are calculated to be 1.528 and 1.417 Å, respectively. The CO bond length of 1.403 Å suggests that a bond order of 1 of the C-O bond, i.e. adsorption causes scission of the two π -bonds of the CO molecule, making it ready for further reaction such as dissociation or hydrogenation. The adsorption energy of CO on *dh*-BN (V_N) is -3.45 eV, which is not far from -4.04 eV or -3.97 eV

reported elsewhere.^{40, 41} The adsorption energy is -3.24 eV with ZPE correction. The Bader charge analysis shows that 2.070 e is transferred from the *dh*-BN to the CO molecule. As shown in the bottom panel of Figure 7a, a sizable electron density accumulation (green region) appeared between the B atom and C atom, and between the B atom and O atom, which verifies the bonding formation of the B-C bond and B-O bond. A loss of electron density (violet region) is shown around the C-O bond, confirming that adsorption weakens the C-O bond by breaking its two π -bonds. In Figure 8a, which contains PDOS of CO adsorption on *dh*-BN (V_N), the orbital mixing between the occupied states of CO molecules (in red line) and the states of B atoms (around the vacancy in blue line). This obvious overlap of states of CO and V_N indicates the strong chemisorption of the CO molecule caused by dangling bonds of the B atoms around the vacancy site. In addition, the peaks in the density of states shift toward the higher energy since a charge transfer takes place from the *dh*-BN surface to the CO molecule.

The strong adsorption of CO on V_N with both C and O bond to Boron atoms of *dh*-BN significantly affect the CO stretching mode. We found that its frequency is 1063.6 cm^{-1} , as compared to that of 2115.0 cm^{-1} of the isolated CO molecule. This is a large shift and reflects the strong bond of CO with the support. In addition, we found that there are several vibrational modes that show strong coupling between CO and *dh*-BN whose frequencies are listed in Table 2 and whose vibrational pattern are shown in Figure 9.

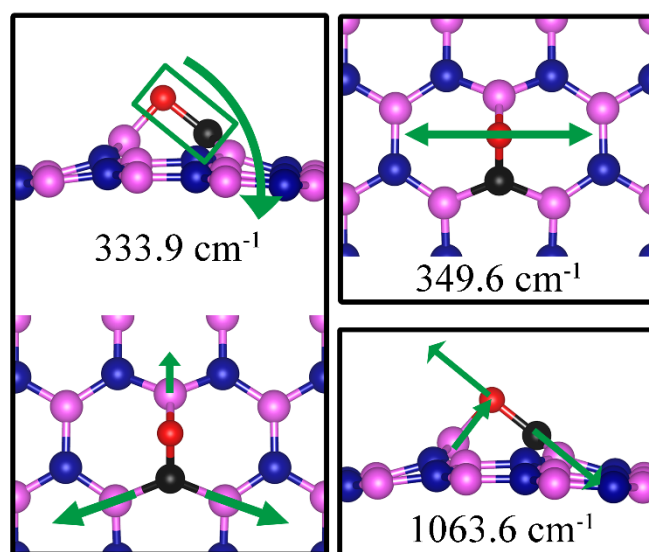


Figure 9 Notable vibrational modes of CO adsorbed on *dh*-BN with V_N . The magenta, blue, black and red balls represent the B, N, C, and O atoms, respectively. Arrows indicate vibrational patterns.

CO adsorption on V_B

The most stable adsorption configuration of CO adsorption on V_B is shown in Figure 7b. In this configuration, CO binds to N1, N2 and N3 atoms in a vertical orientation via C-N bond, which is similar to that previously reported.^{40, 41} C-O bond length increases from 1.143 Å, in gas phase CO, to 1.386 Å, while $d_{(\text{C-N})}$ is found to be 1.501 Å. The CO bond length is larger than that of

a typical bond order 2, but smaller than that of a typical bond order 1. The adsorption energy is -4.54 eV (-4.31 eV with ZPE correction), which is smaller than that of -5.63 or -5.86 eV reported elsewhere.^{40, 41} The difference arises from the form of the exchange-correlation functional used in DFT calculations. The Bader charge analysis shows that about 0.636 e is transferred from the CO molecule to the support. In the bottom panel of Figure 7b, a sizable electron density accumulation (green region) appeared between the C and N atoms, which affirms the strong interaction between the CO molecule and N atoms around the vacancy. A loss of electron density (violet region) surrounds the region between C and O atoms, which shows a weakened C-O bond. In Figure 8b, PDOS of CO adsorption on *dh*-BN at V_B around the Fermi level shows orbital mixing between the occupied states of the CO molecules and orbitals of B atoms, indicating chemisorption of CO on *dh*-BN. Similar to CO adsorption on V_N , the strong adsorption of CO on the V_B defect significantly affects the CO stretching mode. We found that its frequency is 895.5 cm^{-1} , as compared to 2115.0 cm^{-1} of the isolated CO molecule. Such large change is consistent with the elongation of CO bond length upon adsorption. In addition, we found that there are several vibrational modes that show strong coupling between CO and *dh*-BN, whose frequencies are listed in Table 2 and whose displacement patterns are illustrated in Figure 10.

While both studies show a similar adsorption configuration, the difference in binding energies may again be attributed to the exchange correlation functional used in the DFT calculations. For further validating our results, we calculate adsorption energy of CO on SW when it is physisorbed. We found that the physisorption energy is -0.12 eV, indicating that the CO molecule prefers to be in the physisorbed state. We also performed Nudged Elastic Band^{43, 44} calculation between the physisorbed and chemisorbed configurations and found that there is an barrier of 0.57 eV for the physisorbed molecule to adsorb chemically on the SW defect. Bader charge analysis of the chemisorbed CO on SW shows 0.237 e transferred from the surface to CO. The charge density difference plot of CO on *dh*-BN (SW) as shown in the bottom panel of Figure 7c indicates a sizable electron density accumulation (green region) between the B and C atoms, consistent with the formation of B-C bond. However B-C bond length is 1.636 Å, longer than that in the cases of CO on V_N and V_B defects, indicating that the strength of CO binding on *dh*-BN with SW is weaker than that on *dh*-BN with V_N , consistent with calculated positive adsorption energies. PDOS in Figure 8c shows that the conduction band moves toward lower energy and that the valence band shifts toward higher energy, reducing the band gap of *dh*-BN, albeit the energy gap is still large and there is no available electronic state that is at or close to the Fermi level.

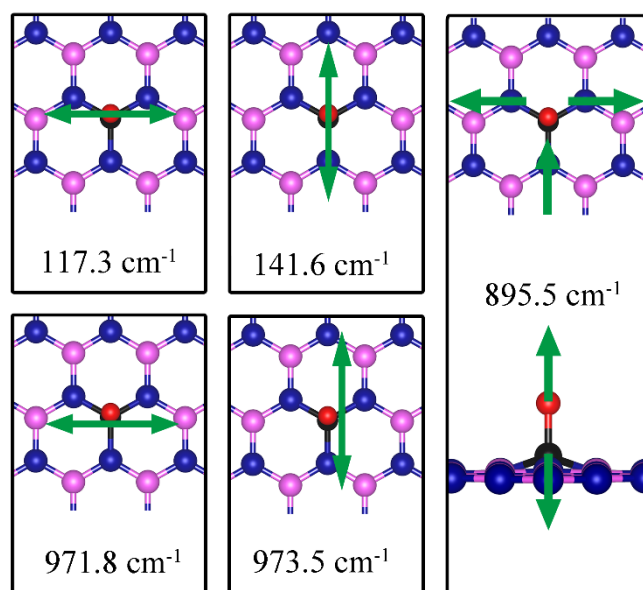


Figure 10 Notable vibrational modes of CO adsorption on *dh*-BN with V_B . The magenta, blue, black and red balls represent the B, N, C, and O atoms, respectively. Arrows indicate vibrational patterns.

CO adsorption on SW

The most energetically favorable configuration of CO adsorption on SW is shown in Figure 7c. CO adsorbs at the B site by pulling the B atom out from the *dh*-BN plane. In this geometry, the bond length of C-O is 1.150 Å and the bond length of C-B is 1.636 Å. The adsorption energy of CO is found to be 0.43 eV (0.44 eV with ZPE correction), which is significantly different from that of -0.58 eV reported in a previous study⁴².

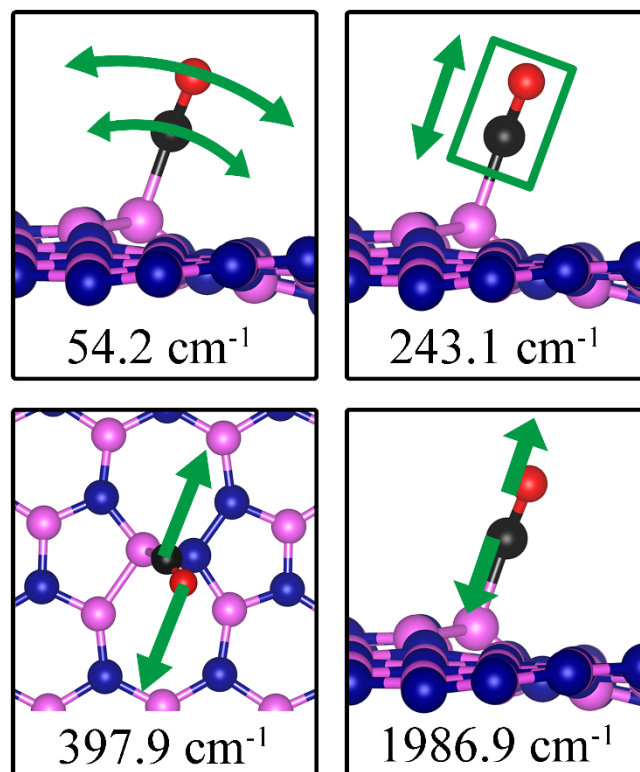


Figure 11 Notable vibrational modes of CO adsorption on *dh*-BN with SW defect. The magenta, blue, black and red balls represent the B, N, C, and O atoms, respectively. Arrows indicate vibrational patterns. The rectangular encloses the atoms that concertedly move.

As the strength of the adsorption of CO on SW is much reduced as compared to that on V_B and V_N , the CO stretching frequency is found to be 1987 cm^{-1} . This mode is softer than that in isolated CO molecule due to the reduction in strength of CO bond and its elongation upon adsorption. In addition, we found that there are several vibrational modes that show strong contribution from C and O movements whose frequencies are listed in Table 2 and whose displacement patterns are shown in Figure 11.

CO adsorption on B_N

Figure 7d shows the energetically favored configuration of the adsorption of CO on *dh*-BN with B_N , in which CO binds perpendicularly on top of the central B atom (labeled as B4) with an adsorption energy of -2.53 eV (-2.45 eV with ZPE correction). The calculated bond length $d_{(C-B)}$ and $d_{(C-O)}$ are 1.444 \AA and 1.163 \AA (elongated by $\sim 0.03\text{ \AA}$ from that in gas-phase), respectively. CDD plot of CO on *dh*-BN with B_N shown in the bottom panel of Figure 7d indicates a sizable electron density accumulation (green region) between the B and C atoms, confirming the strong interaction between the CO molecule and its neighboring B atoms around the defect area. A small loss of electron density (violet region) is seen over the C–O bond, indicating weakening of the C–O bond, consistent with its elongation (from 1.134 \AA in gas phase to 1.163 \AA). A large loss of electron density (violet region) is found over the B4–B1, B4–B2 and B4–B3 bonds, suggesting that the bonds are weakened on CO adsorption. Bader charge analysis shows a net 0.470 e transferred from *dh*-BN (with B_N) to CO. After CO adsorption on *dh*-BN with B_N , the density of states peaks shift toward lower energy, as shown in Figure 8d. More importantly, the defect states merge with the valence and conduction bands, suggesting the absence of dangling bonds and the inability of more molecules to adsorb, thus passivating the catalytic activity of *dh*-BN with B_N .

The stretching frequency of the adsorbed CO molecule on *dh*-BN with B_N is found to be 1999 cm^{-1} . This mode is slightly softer than that in isolated CO molecule commensurate with small reduction in strength of the CO bond as a result of slight elongation upon adsorption. In addition, we found that there are several vibrational modes that show strong coupling between CO and *dh*-BN, vibrational patterns of six of which are shown in as shown in Figure 12.

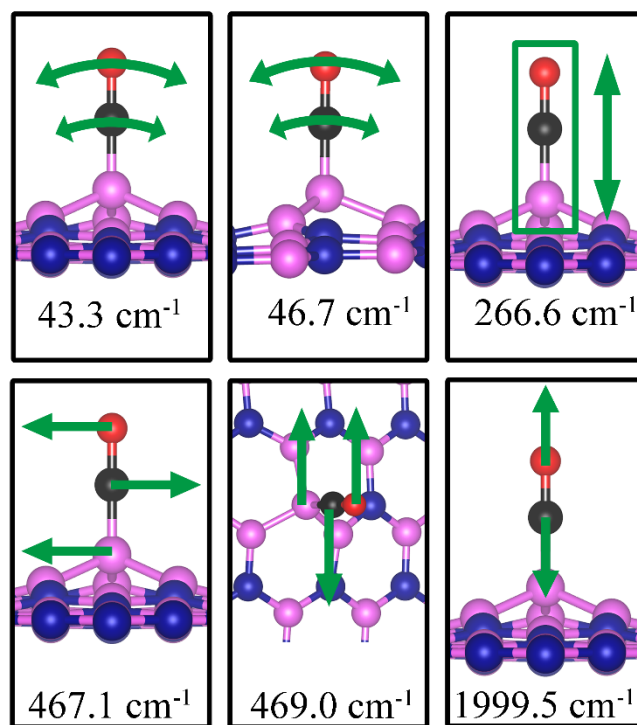


Figure 12 Notable vibrational modes of CO adsorption on *dh*-BN with B_N . The magenta, blue, black and red balls represent the B, N, C, and O atoms, respectively. Arrows indicate vibrational patterns. The rectangular encloses the atoms that are concertedly move together.

CO₂ on *dh*-BN

The geometry structure of CO₂ adsorption on the V_N , V_B , SW, and B_N are shown in Figure 13. The corresponding adsorption energies and geometric parameters are summarized in Table 3.

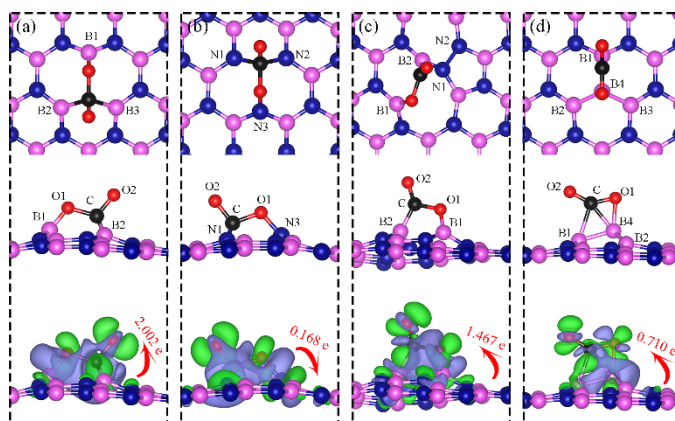


Figure 13 Top and side views of the most energetically favorable configurations of adsorbed CO₂ on the *dh*-BN with a) V_N , b) V_B , c) SW, and d) B_N . The magenta, blue, black and red balls represent the B, N, C, and O atoms, respectively. The top and middle panel shows the top and side views, respectively. Bottom: the corresponding side views of the geometric structures with the charge density difference plot. The green and violet isosurfaces with iso-value of $\pm 0.003\text{ e/\AA}^3$, represent the accumulation and depletion of electron, respectively. The red arrow shows the electron transfer in direction and value.

Table 3 The adsorption energy without (E_{ads}) and with (E'_{ads}) ZPE correction and geometrical parameters for adsorption of CO_2 on dh -BN.

Defects	E_{ads} (eV)	E'_{ads} (eV)	Bond length (Å) and Bond angle (°)	Notable frequencies (cm ⁻¹)
V_N	-1.83	-1.73	$d_{(\text{C-O}1)}=1.438$, $d_{(\text{C-O}2)}=1.311$, $d_{(\text{C-B}2)}=1.672$, $d_{(\text{O}1-\text{B}1)}=1.382$, $\theta_{(\text{O}1-\text{C-O}2)}=113.7^\circ$	95.7, 250.7, 253.4, 373.2, 667.6, 1193.2, 1296.6
V_B	-0.62	-0.48	$d_{(\text{C-O}1)}=1.409$, $d_{(\text{C-O}2)}=1.353$, $d_{(\text{C-N}1)}=1.496$, $d_{(\text{O}1-\text{N}3)}=1.446$, $\theta_{(\text{O}1-\text{C-O}2)}=107.1^\circ$	141.8, 1006.0, 1073.1
SW	0.49	0.51	$d_{(\text{C-O}1)}=1.405$, $d_{(\text{C-O}2)}=1.209$, $d_{(\text{C-B}2)}=1.582$, $d_{(\text{O}1-\text{B}1)}=1.412$, $\theta_{(\text{O}1-\text{C-O}2)}=121.9^\circ$	124.6, 157.8, 753.1, 839.5, 1225.0, 1715.6
B_N	-0.10	-0.10	$d_{(\text{C-O}1)}=1.273$, $d_{(\text{C-O}2)}=1.206$, $d_{(\text{C-B}1)}=1.989$, $d_{(\text{C-B}4)}=1.807$, $d_{(\text{O}1-\text{B}4)}=1.661$, $\theta_{(\text{O}1-\text{C-O}2)}=139.6^\circ$	103.6, 612.2, 1081.5, 1802.2

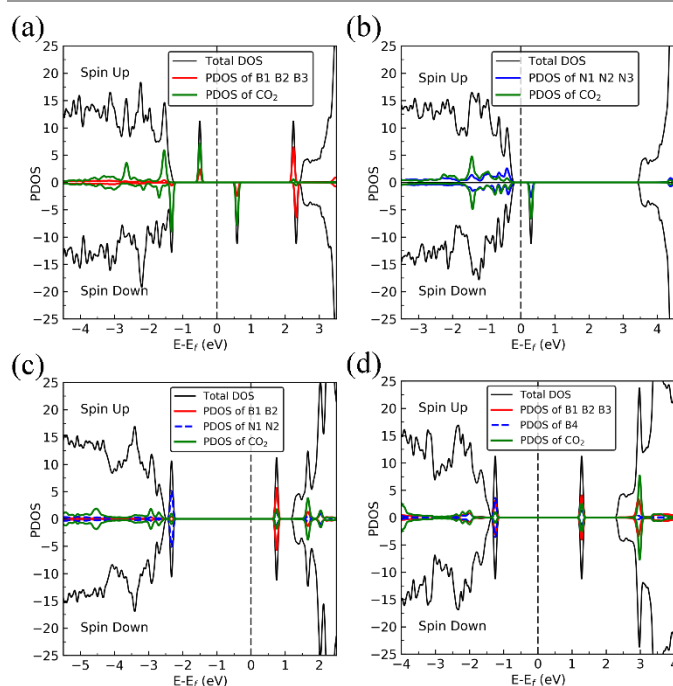


Figure 14 Spin-polarized total density of states (TDOS) (black line), spin-polarized PDOS of defect area in (red line or blue line) and spin-polarized PDOS adsorbed CO_2 (green line) of CO_2 - dh -BN with (a) V_N , (b) V_B , (c) SW, and (d) B_N , respectively. The position of the Fermi level (EF) is indicated by dashed line.

CO_2 adsorption on V_N

On dh -BN with V_N , CO_2 binds at the defect sites, with an adsorption energy of -1.83 eV (-1.73 eV with ZPE correction), indicating a strong chemisorption of the CO_2 molecule at the

vacancy site. As shown in Figure 13a, the adsorption pulls B1, B2 and B3 atoms slightly out of the dh -BN plane and the CO_2 molecule lies in the proximity of three boron sites near the vacancy with bond lengths, $d_{(\text{O}1-\text{B}1)}$, and $d_{(\text{C-B}2)}$ ($d_{(\text{C-B}3)}$), of 1.382 and 1.672 Å, respectively. The molecule is bent with the O1-C-O2 angle of 107.1°. The bond lengths, $d_{(\text{C-O}1)}$ and $d_{(\text{C-O}2)}$, are 1.438 and 1.311 Å, respectively (both are longer than that of 1.172 Å of gas phase CO_2), indicating that the original C-O bonds are stretched upon interaction between CO_2 and dh -BN with V_N . Bader charge analysis shows that about 2.002 e transferred from dh -BN to the CO_2 molecule. CDD plot of CO_2 on dh -BN with V_N , shown in the bottom panel of Figure 13a, indicates a sizable electron density accumulation (green region) appearing between the B2 (B3) and C atoms and between the B1 and O atoms, consistent with the formation of new bonds B2(B3)-C and B1-C. A loss of electron density (violet region) between C-O is also consistent with the elongation and weakening of the C-O bond. PDOS shown in Figure 14a indicates overlaps, i.e. hybridizations, between states of CO_2 molecule and the states of B atoms, indicating the chemisorption of CO_2 on the dh -BN with V_N and the strong interaction between the molecule and the dh -BN sheet. We also find that the defect states, i.e. the ones near the Fermi level, are mostly contributed from CO_2 and shifted toward lower energy, closer to VBM. This phenomenon indicates that the defect states have migrated (transferred) to the adsorbed CO_2 molecules.

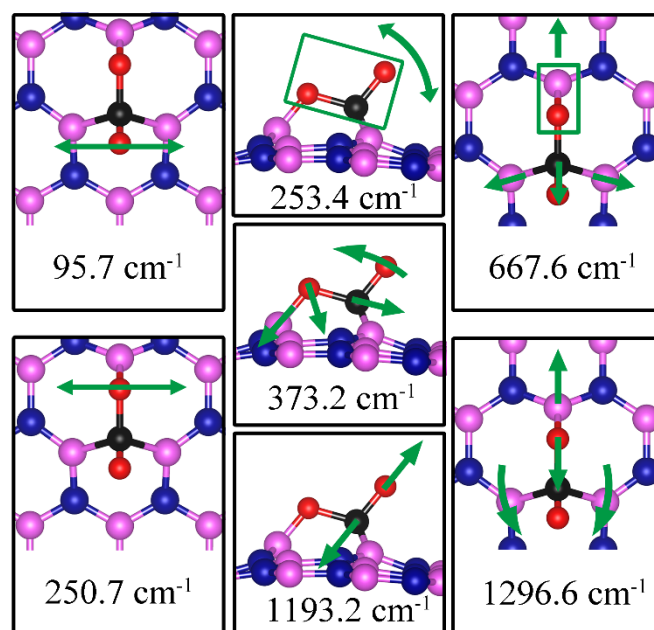


Figure 15 Notable vibrational modes of CO_2 adsorption on dh -BN with V_N . The magenta, blue, black and red balls represent the B, N, C, and O atoms, respectively. Arrows indicate vibrational patterns. The rectangular encloses the atoms that move together.

Since CO_2 adsorbs on dh -BN with a bent configuration, the normal vibrational mode of CO_2 molecule (symmetric stretching, antisymmetric stretching, bending) are absent. Instead, we found few notable vibrational modes that include contributions from the adsorbed CO_2 molecules, as shown in

Figure 15, with their frequencies listed in Table 3. Among them, the stretching mode of the C–O bond is of particular interest as it is infra-red active and its frequency is 1193.2 cm^{-1} , which is different from that (1063.6 cm^{-1}) of the adsorbed CO molecule on the same defect.

CO₂ adsorption on V_B

On *dh*-BN with V_B, CO₂ binds at the N sites with an adsorption energy of -0.62 eV (-0.48 eV with ZPE correction). Figure 13b shows the corresponding adsorption configuration, in agreement with that reported in previous work,⁴⁵ which also reported a binding energy of -0.62 eV . In this configuration, CO₂ lies in between the three N sites with bond lengths, $d_{(\text{C-N}_1)}$ and $d_{(\text{O-N}_3)}$, of 1.496 \AA and 1.446 \AA , respectively. The bond lengths, $d_{(\text{C-O}_1)}$ and $d_{(\text{C-O}_2)}$, are 1.409 \AA and 1.353 \AA (longer than that 1.172 \AA of an isolated molecule), respectively, indicating weakening of the C–O bonds. The Bader charge analysis shows 0.168 e transferred from the molecule to the *dh*-BN. CDD plot of CO₂ on *dh*-BN with V_B shown in Figure 13b shows a sizable electron density accumulation (green region) between the N and C atoms, confirming the formation of N–C bond, and a loss of electron density (violet region) between the C and O atoms, consistent with the weakening of C–O bonds. PDOS shown in Figure 14b indicates hybridizations of electronic states of the adsorbed CO₂ molecule and defects states of *dh*-BN with V_B, confirming the chemisorption of the molecule. It also suggests that the dangling bonds at the N atoms at defect site of *dh*-BN are partially saturated, as the contributions of N atoms to the defect states are reduced as compared to that in the absence of CO₂.

Similar to the case of CO₂ adsorbed on the *dh*-BN with V_N, the molecule is found to adsorb with a bent configuration on V_B, thus the normal vibrational mode of CO₂ molecule (symmetric stretching, antisymmetric stretching, bending) are not present. We found again three notable vibrational modes that show contributions from the adsorbed CO₂ molecules, as shown in Figure 16, with their frequencies listed in Table 3. The stretching mode of the C–O bond that points outward from *dh*-BN has a frequency of 1006.0 cm^{-1} . This mode is also infrared-active and we assign this mode as a signature for the identification of the adsorption of CO₂ on the *dh*-BN with V_N.

CO₂ adsorption on SW

On *dh*-BN with SW, CO₂ binds at two B sites with adsorption energy of $+0.36\text{ eV}$ (0.44 eV with ZPE correction) indicating that the adsorption is endothermic. As shown in Figure 13c, the adsorbed CO₂ pulls the B atom out of the *dh*-BN plane. The two C–O bond lengths are found to be with 1.405 \AA (C–O₁) and 1.209 \AA (C–O₂). The bond lengths, $d_{(\text{C-B}_2)}$ and $d_{(\text{O}_1\text{-B}_1)}$, are 1.582 \AA and 1.412 \AA , respectively. Bader charge analysis shows 1.456 e transferred from *dh*-BN with SW to the molecule. CDD plot of CO₂ on *dh*-BN with SW, as shown in Figure 13c, indicates a sizable electron density accumulation (green region) appeared between the B and C atoms and between the B and O atoms and, suggesting covalent bond formation between the pairs of atoms and a large loss of electron density in the region between the B₁ and B₂ atoms, indicating weakening of the B–B bond of the defect. PDOS, as shown in Figure 14c, indicates that the conduction band moves toward lower energy while the valence band shifts toward higher energy, similar to case of CO on *dh*-BN with SW. It also shows that contributions from B₁, B₂, N₁, and N₂ atoms to the defect states are still dominant while only small contribution of the adsorbed CO₂ is observed, implying a weak interaction between CO₂ and *dh*-BN with SW. This weak interaction and the energy-costs for bending the CO₂ molecule and for breaking B–B bond at the SW are the reasons why the adsorption of CO₂ on *dh*-BN with SW is endothermic.

Even though the adsorption is endothermic, we have calculated the vibrational frequencies for the above configurations. We found four notable vibrational modes that are localize at or near the adsorbed CO₂. Their vibrational patterns are shown in Figure 17 and their frequencies are listed in Table 3. In this configuration, we found that the stretching mode of the C–O bond that points outward from the defect has a frequency of 1715.6 cm^{-1} . This mode is infrared active and could be the signature of this adsorption configuration.

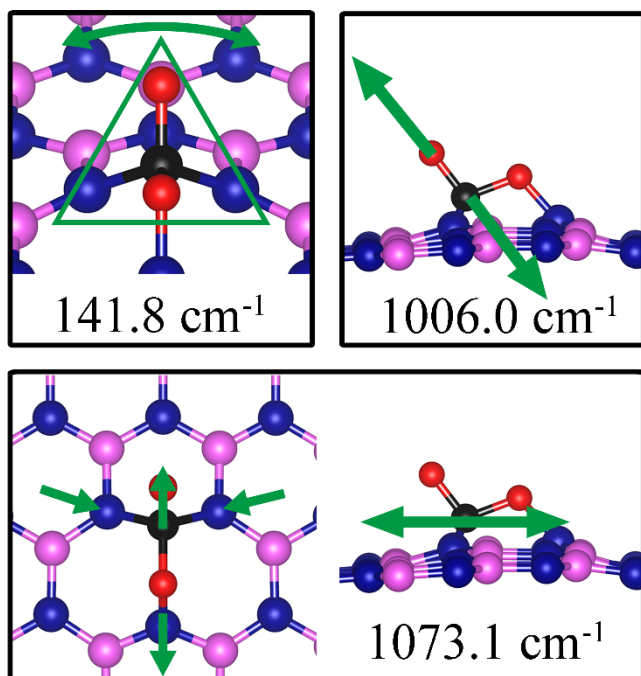


Figure 16 Notable vibrational modes of CO₂ adsorption on *dh*-BN with V_B. The magenta, blue, black and red balls represent the B, N, C, and O atoms, respectively. Arrows indicate vibrational patterns. The trapezium-like shape in 141.8 cm^{-1} mode encloses the group of atoms that concertedly vibrate together.

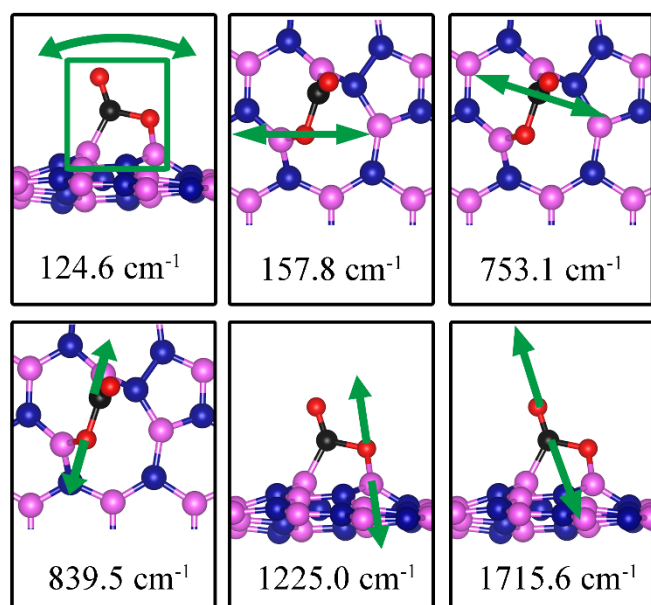


Figure 17 Notable vibrational modes of CO₂ adsorption on *dh*-BN with SW. The magenta, blue, black and red balls represent the B, N, C, and O atoms, respectively. Arrows indicate vibrational patterns. The square in 124.6 cm⁻¹ mode figure (left) encloses all atoms that concertedly vibrate together.

CO₂ adsorption on B_N

On *dh*-BN with B_N as shown in Figure 13d, the adsorbed CO₂ molecule undergoes structural distortion to a bent geometry with bond order reduction of C–O bonds in a way similar to that reported for CO₂ chemisorption on B-rich BNNTs.³⁹ The O1–C–O2 bond angle is 139.6°, and the C–O1 and C–O2 bonds are significantly elongated to 1.206 and 1.273 Å, respectively, indicating bond-order reductions. The B4 atom at the defect site is pulled out of *dh*-BN plane considerably by ~1 Å. The adsorption energy of CO₂ adsorbed at the B_N is found to be -0.10 eV (ZPE correction does not change the value), which is significantly lower than that of -0.74 eV reported for B-rich BNNTs.³⁹ The Bader charge analysis shows 0.710 e is transferred from the *dh*-BN to the molecule. CDD plot of CO₂ on *dh*-BN with B_N, as shown in Figure 13d, indicates a sizable electron density accumulation (green region) in the region between the B and C atoms and between the B and O atoms and a large loss of electron density (violet region) in the region between the B1 atom and B2 atom, indicating the weakening of B–B bond. The CO₂ adsorption on *dh*-BN with B_N thus cause the density of states to shift toward higher energy (Figure 14d), consistent with direction of electron transfer from *dh*-BN to the CO₂ molecule.

We found two notable vibrational modes that display large contribution from the adsorbed CO₂ molecule. The displacement patterns of these modes are shown in Figure 18 and their frequencies are listed in Table 3. The stretching mode of the C–O bond that points outward from the *dh*-BN plane has a frequency of 1802.2 cm⁻¹. This mode is infrared active and we assign it as the signature of the adsorption configuration discussed above.

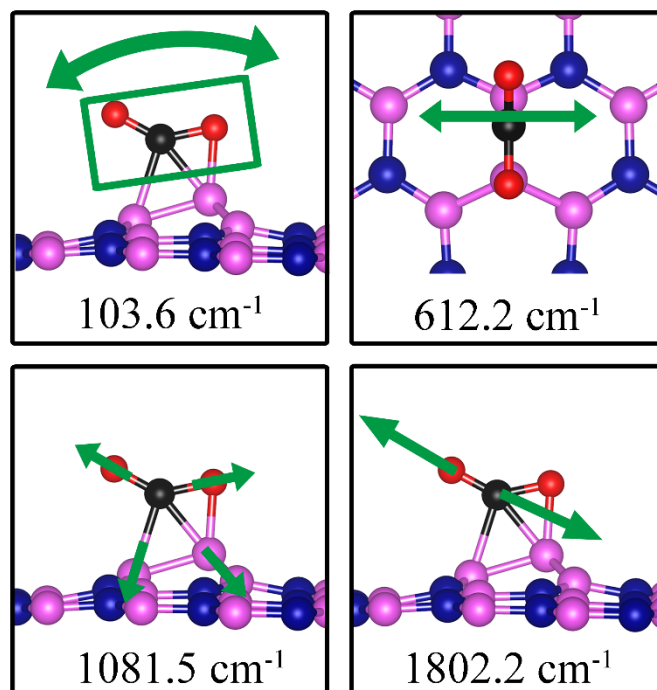


Figure 18 Notable vibrational modes of CO₂ adsorption on *dh*-BN with B_N. The magenta, blue, black and red balls represent the B, N, C, and O atoms, respectively. Arrows indicate vibrational patterns. The rectangular in the left figure encloses atoms that concertedly vibrate together.

Catalytic Properties of *dh*-BN

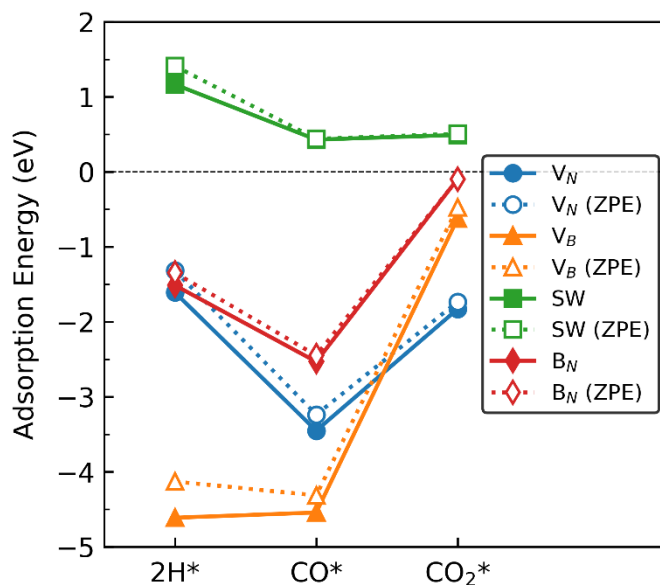


Figure 19 Adsorption energy of 2H, CO, and CO₂ on the *dh*-BN with (a) V_N, (b) V_B, (c) SW, and (d) B_N, shown with circle, triangle, square, and diamond markers, respectively. Values without and with ZPE corrections are shown in solid and empty markers, respectively. The markers for each defect types are connected with solid or dotted lines for guiding the eyes.

This section discusses the implication of our finding for catalytic application of *dh*-BN for hydrogenations of CO and CO₂. To facilitate these reactions, it is important that co-adsorption of CO or CO₂ with H₂ be feasible on the defects. Our results presented above suggest that H atoms can be chemisorbed on the defects while molecular adsorption leads to physisorption. Figure 19 shows comparison of the adsorption energy of 2 H, CO, and CO₂. On *dh*-BN with SW, adsorptions of 2H, CO and CO₂ on SW are endothermic (positive adsorption energies), suggesting that these adsorptions are not favored, and thus hydrogenation of CO or CO₂ are not feasible on such type of defect. On *dh*-BN with V_B, on the other hand, adsorption energies of 2 H and CO are similar and in the range from -4 to -5 eV, suggesting rather strong adsorption. Such strong adsorption, however, often lead to difficulties in the removal or diffusion of the adsorbates (reactants) and for co-adsorption to occur. It is most likely that the V_B sites will remain occupied by H or CO during a reaction, thus deactivating the site. Moreover, with the V_B defect adsorption of CO₂ is substantially weaker than that of 2 H, making it less likely should the site is occupied by 2 H. We thus conclude that *dh*-BN with V_B is also not suitable for CO₂ hydrogenation. Similarly, on *dh*-BN with B_N, adsorption of CO₂ is a weak chemisorption, implying that CO₂ could easily desorb before it would have the opportunity to react with other species under reaction condition. On the other hand, the strength of 2 H and CO adsorptions are similar and strong for stable adsorptions. However, the PDOS of adsorption of 2H and CO on *dh*-BN with B_N, as shown in Figure 5 and Figure 8, respectively, do not show any mid-gap state, indicating there is no dangling bond in the band gap for more molecules to adsorb. The above lead us to surmise that for such a defect co-adsorption is less likely to occur. The situation is different for *dh*-BN with V_N. With this particular defect we find that while the binding of CO is strong (adsorption energy of -3.24 eV with ZPE correction) — suggesting that CO could occupy and deactivate the site — the adsorption energies of 2H and CO₂ are in a similar range that is not too strong to block active sites or not too weak to be stable. The above comparisons lead us to suggest that *dh*-BN with V_N could be a potential catalyst for CO₂ hydrogenation. This is in agreement with similar conclusion obtained for the hydrogenation of olefins.⁶

Conclusions

Our systematic analysis of the electronic structure and vibrational dynamics of syngas molecules adsorbed on defect-laden single-layer *h*-BN, using density functional theory based calculations, has allowed us to make a distinction among four types defects (V_N, V_B, SW, and B_N) that we considered. We find that CO and CO₂ molecules chemisorb on *dh*-BN for each of the four defect types, while H₂ only physisorbs on these defects. On the other hand, atomic hydrogen adsorbs on the defects. The above conclusions are also supported by analysis of the partial density of electronic states and charge density difference plots. In addition, our calculations of vibrational frequencies for the considered adsorptions point to a number of notable vibrational modes that could help in the identification of defect type,

through their experimental examination such as infrared absorption spectroscopy of the adsorbed molecules on *dh*-BN. Our results provide fundamental insights into the interaction of syngas molecules and *dh*-BN through which we can prescreen the defect type that would make the basal plane of the *dh*-BN catalytically active for CO and CO₂ hydrogenation reactions. In particular, by comparing the adsorption energy of the molecules on *dh*-BN with each of the four defect types, accompanied with analysis on their electronic and geometric structures, we suggest that *dh*-BN with V_N (nitrogen vacancy) as a good candidate catalyst for CO₂ hydrogenation. We await experimental results that validate our findings.

On a more general note, although we have focused mostly on the chemical activity of defect-laden *h*-BN in this work, as we mention in the introduction, this interesting low-dimensional material is also being proposed as a single photon emitter in which defects play a major and their characterization is a challenge. Our work provides signatures in the vibrational modes of the adsorbed molecules that are strikingly different for the four defect types and thus could serve to identify them in experiments such as infra-red absorption spectroscopy which is commonly available. We hope our work encourages colleagues to undertake such measurement as probe of the nature of the defect in *h*-BN that gives rise to several novel properties.

Conflicts of interest

There are no conflicts to declare.

Acknowledgments

It is a pleasure to submit this work to a volume dedicated to Peter Toennies with whom TSR has had many fruitful scientific interactions over the years. She also remembers very fondly discussions with JPT at Schloss Ringberg and a particular challenging hike in the area which ended well. We also thank Richard Blair and Hannah Stern for many helpful discussions. This work was supported in part by the U.S. Department of Energy, under Grant DE-FG02-07ER15842. The DFT calculations were performed in part using the computing resources at STOKES in the Advanced Research Computing Center at University of Central Florida, at the National Energy Research Scientific Computing Center (NERSC).

Notes and references

1. Y. Lin and J. W. Connell, *Nanoscale*, 2012, **4**, 6908-6939.
2. K. Watanabe, T. Taniguchi and H. Kanda, *Nat Mater*, 2004, **3**, 404-409.
3. R. Decker, Y. Wang, V. W. Brar, W. Regan, H.-Z. Tsai, Q. Wu, W. Gannett, A. Zettl and M. F. Crommie, *Nano Lett.*, 2011, **11**, 2291-2295.
4. Y. Li, Y. Rao, K. F. Mak, Y. You, S. Wang, C. R. Dean and T. F. Heinz, *Nano Lett*, 2013, **13**, 3329-3333.
5. J. Di, J. Xia, M. Ji, B. Wang, S. Yin, Q. Zhang, Z. Chen and H. Li, *Applied Catalysis B: Environmental*, 2016, **183**, 254-262.
6. D. J. Nash, D. T. Restrepo, N. S. Parra, K. E. Giesler, R. A. Penabade, M. Aminpour, D. Le, Z. Li, O. K. Farha, J. K. Harper, T. S. Rahman and R. G. Blair, *ACS Omega*, 2016, **1**, 1343-1354.
7. J. T. Grant, C. A. Carrero, F. Goeltl, J. Venegas, P. Mueller, S. P. Burt, S. E. Specht, W. P. McDermott, A. Chiericato and I. Hermans, *Science*, 2016, **354**, 1570-1573.
8. T. T. Tran, K. Bray, M. J. Ford, M. Toth and I. Aharonovich, *Nat. Nanotechnol.*, 2016, **11**, 37-41.
9. J. Feng, H. Deschout, S. Caneva, S. Hofmann, I. Lončarić, P. Lazić and A. Radenovic, *Nano Lett.*, 2018, **18**, 1739-1744.
10. R. Bourrellier, S. Meuret, A. Tararan, O. Stéphane, M. Kociak, L. H. G. Tizei and A. Zobelli, *Nano Lett.*, 2016, **16**, 4317-4321.
11. M. Topsakal, E. Aktürk and S. Ciraci, *Phys. Rev. B*, 2009, **79**, 115442.
12. D. Le, T. B. Rawal and T. S. Rahman, *J. Phys. Chem. C*, 2014, **118**, 5346-5351.
13. T. B. Rawal, D. Le and T. S. Rahman, *J. Phys.: Condens. Matter* 2017, **29**, 415201.
14. T. B. Rawal, D. Le and T. S. Rahman, *J. Phys. Chem. C*, 2017, **121**, 7282-7293.
15. P. E. Evans, H. K. Jeong, Z. Hooshmand, D. Le, T. B. Rawal, S. N. Alvililar, L. Bartels, T. S. Rahman and D. P. A., *J. Phys. Chem C*, 2018, **122** 10042-10049.
16. C. S. Merida, D. Le, E. M. Echeverria, A. E. Nguyen, T. B. Rawal, S. Naghibi Alvililar, V. Kandyba, A. Al-Mahboob, Y. Losovyj, K. Katsiev, M. D. Valentin, C.-Y. Huang, M. J. Gomez, I. H. Lu, A. Guan, A. Barinov, T. S. Rahman, P. A. Dowben and L. Bartels, *J. Phys. Chem. C*, 2018, **122**, 267-273.
17. H. Li, C. Tsai, A. L. Koh, L. Cai, A. W. Contryman, A. H. Fragapane, J. Zhao, H. S. Han, H. C. Manoharan, F. Abild-Pedersen, J. K. Nørskov and X. Zheng, *Nat Mater*, 2016, **15**, 48-53.
18. B. Huang and H. Lee, *Phys. Rev. B*, 2012, **86**, 245406
19. C. Jin, F. Lin, K. Suenaga and S. Iijima, *Phys. Rev. Lett.*, 2009, **102**, 195505.
20. R. Schimmenti, R. Cortese, D. Duca and M. Mavrikakis, *Chemcatchem*, 2017, **9**, 1610-1620.
21. S. Lin, X. Ye, R. S. Johnson and H. Guo, *J. Phys. Chem. C*, 2013, **117**, 17319-17326.
22. X. Liu, T. Duan, C. Meng and Y. Han, *RSC Adv.*, 2015, **5**, 10452-10459.
23. Q. Sun, Z. Li, D. J. Searles, Y. Chen, G. M. Lu and A. Du, *J. Am. Chem. Soc.*, 2013, **135**, 8246-8253.
24. A. L. Gibb, N. Alem, J. H. Chen, K. J. Erickson, J. Ciston, A. Gautam, M. Linck and A. Zettl, *J. Am. Chem. Soc.*, 2013, **135**, 6758-6761.
25. C. K. Oliveira, E. F. A. Gomes, M. C. Prado, T. V. Alencar, R. Nascimento, L. M. Malard, R. J. C. Batista, A. B. de Oliveira, H. Chacham, A. M. de Paula and B. R. A. Neves, *Nano Res.*, 2015, **8**, 1680-1688.
26. I. N. Remediakis, F. Abild-Pedersen and J. K. Nørskov, *J. Phys. Chem. B*, 2004, **108**, 14535-14540.
27. Y. Choi and P. Liu, *J. Am. Chem. Soc.*, 2009, **131**, 13054-13061.
28. Y. Yang, J. Evans, J. A. Rodriguez, M. G. White and P. Liu, *Phys. Chem. Chem. Phys.*, 2010, **12**, 9909-9917.
29. H. Wu, X. Fan and J.-L. Kuo, *Int. J. Hydrogen Energy*, 2012, **37**, 14336-14342.
30. W. Wang, S. Wang, X. Ma and J. Gong, *Chem. Soc. Rev.*, 2011, **40**, 3703-3727.
31. P. Giannozzi, S. Baroni, N. Bonini, M. Calandra, R. Car, C. Cavazzoni, D. Ceresoli, G. L. Chiarotti, M. Cococcioni, I. Dabo, A. Dal Corso, S. de Gironcoli, S. Fabris, G. Fratesi, R. Gebauer, U. Gerstmann, C. Gougoussis, A. Kokalj, M. Lazzeri, L. Martin-Samos, N. Marzari, F. Mauri, R. Mazzarello, S. Paolini, A. Pasquarello, L. Paulatto, C. Sbraccia, S. Scandolo, G. Sclauzero, A. P. Seitsonen, A. Smogunov, P. Umari and R. M. Wentzcovitch, *Journal of physics. Condensed matter : an Institute of Physics journal*, 2009, **21**, 395502.
32. P. E. Blöchl, *Physical Review B*, 1994, **50**, 17953-17979.
33. G. Kresse and D. Joubert, *Phys. Rev. B*, 1999, **59**, 1758-1775.
34. K. Lee, E. D. Murray, L. Z. Kong, B. I. Lundqvist and D. C. Langreth, *Phys. Rev. B*, 2010, **82**, 081101.
35. W. Tang, E. Sanville and G. Henkelman, *J. Phys.: Condens. Matter*, 2009, **21**, 084204.
36. R. F. Bader, *Acc. Chem. Res.*, 1985, **18**, 9-15.
37. A. Togo and I. Tanaka, *Scripta Mater.*, 2015, **108**, 1-5.
38. R. Wang, J. Yang, X. Wu and S. Wang, *Nanoscale*, 2016, **8**, 8210-8219.
39. H. Choi, Y. C. Park, Y. H. Kim and Y. S. Lee, *J. Am. Chem. Soc.*, 2011, **133**, 2084-2087.
40. Z. L. Liu, Q. Z. Xue, T. Zhang, Y. H. Tao, C. C. Ling and M. X. Shan, *J. Phys. Chem. C*, 2013, **117**, 9332-9339.
41. K. Mao, L. Li, W. Zhang, Y. Pei, X. C. Zeng, X. Wu and J. Yang, *Sci Rep*, 2014, **4**, 5441.
42. Y.-H. Zhang, K.-G. Zhou, X.-C. Gou, K.-F. Xie, H.-L. Zhang and Y. Peng, *Chem. Phys. Lett.*, 2010, **484**, 266-270.
43. G. Henkelman and H. Jonsson, *J. Chem. Phys.*, 2000, **113**, 9978-9985.
44. G. Henkelman, B. P. Uberuaga and H. Jonsson, *J. Chem. Phys.*, 2000, **113**, 9901-9904.
45. Y. Jiao, A. Du, Z. Zhu, V. Rudolph, G. Q. Lu and S. C. Smith, *Catal. Today*, 2011, **175**, 271-275.